

Extreme mechanical resilience of self-assembled nanolabyrinthine materials

Carlos M. Portela^a, A. Vidyasagar^a, Sebastian Krödel^b, Tamara Weissenbach^b, Daryl W. Yee^a, Julia R. Greer^a, and Dennis M. Kochmann^{a,b,1}

^aDivision of Engineering and Applied Science, California Institute of Technology, Pasadena, CA 91125; and ^bDepartment of Mechanical and Process Engineering, ETH Zürich, 8092 Zürich, Switzerland

Edited by John W. Hutchinson, Harvard University, Cambridge, MA, and approved February 6, 2020 (received for review September 26, 2019)

Low-density materials with tailorable properties have attracted attention for decades, yet stiff materials that can resiliently tolerate extreme forces and deformation while being manufactured at large scales have remained a rare find. Designs inspired by nature, such as hierarchical composites and atomic lattice-mimicking architectures, have achieved optimal combinations of mechanical properties but suffer from limited mechanical tunability, limited long-term stability, and low-throughput volumes that stem from limitations in additive manufacturing techniques. Based on natural self-assembly of polymeric emulsions via spinodal decomposition, here we demonstrate a concept for the scalable fabrication of nonperiodic, shell-based ceramic materials with ultralow densities, possessing features on the order of tens of nanometers and sample volumes on the order of cubic centimeters. Guided by simulations of separation processes, we numerically show that the curvature of self-assembled shells can produce close to optimal stiffness scaling with density, and we experimentally demonstrate that a carefully chosen combination of topology, geometry, and base material results in superior mechanical resilience in the architected product. Our approach provides a pathway to harnessing self-assembly methods in the design and scalable fabrication of beyond-periodic and nonbeam-based nano-architected materials with simultaneous directional tunability, high stiffness, and unsurpassed recoverability with marginal deterioration.

self-assembly | metamaterial | damage tolerance | resilience | anisotropy

The design of architected cellular materials to date has heavily relied on truss-based geometries, which achieve desirable mechanical properties, such as high stiffness- or strength-to-density ratios (1–6), flaw tolerance (7), high energy absorption (8), and vibration mitigation (9). Truss-based architectures, like open cell foams, engage their structural members in both stretching and bending, the latter being particularly prominent in nonslender beam networks regardless of architecture (10, 11). This compliant deformation mode is responsible for poor stiffness-to-density scaling (2, 4, 8) (i.e., the effective truss stiffness decreases strongly—faster than linearly—with decreasing density and weight). Additionally, truss lattices have relied on symmetry, periodicity, and scarcity of defects (10) to achieve their ideal mechanical properties. Symmetry-breaking defects in these materials, emerging in virtually any fabrication route, can undermine their strength and stiffness as well as their resilience on sustained loading (12–15). As an alternative, plate- and shell-based geometries have been shown to mitigate bending and to reach theoretical stiffness bounds (16, 17) by improving the load distribution within their members as compared with trusses. Unfortunately, those usually exhibit poor recoverability since most truss- and plate-based designs suffer from stress concentrations at junctions, which commonly leads to localized permanent damage and material failure under applied loads (8, 15). As an apparent remedy, smooth shell architectures, such as triply periodic minimal surfaces (TPMS) (18), avoid sharp junctions and

attain high stiffness owing to double curvature in its components. This concept of nonzero Gaussian curvature, first introduced by Gauss in his *Theorema Egregium*, explains the mechanical benefits of doubly curved surfaces (19) and has been identified as providing rigidity to natural structures, such as egg shells (20) and plant leaves (21). Recently, applications of this concept have led to smooth shell architectures that achieve stretching-dominated behavior and have superior energy absorption capabilities as compared with trusses (22–25).

The beneficial mechanical properties of those synthesized truss-, plate-, and shell-based architected materials are largely enabled by the periodicity of symmetric unit cells, which can be susceptible to symmetry-breaking defects such as strut/wall waviness, varying cross-section, and offset nodes (8, 10, 12) as well as the effects of free boundaries (18, 26). Moreover, such periodic architectures are typically achievable only through additive manufacturing techniques at small scales, which are nonscalable and often introduce defects, inevitably resulting in lower than theoretical strength and stiffness. As a point of departure from periodicity, materials that are formed through natural evolution processes like nanoporous foams (27) are often nonperiodic and composed of bicontinuous networks of smooth, doubly curved solid morphologies. Architectures obtained through these processes are also typically isotropic and can be particularly resilient against defects (28). Tuning these natural morphologies, with the potential for direction-dependent properties, can be achieved

Significance

Nano- and microarchitected materials to date have relied on additive manufacturing techniques to produce beam-, plate-, and shell-based architectures that achieve highly desired mechanical properties while being limited to low-throughput volumes as well as to periodic and symmetric designs that deteriorate if symmetry-breaking defects are present. Here, we demonstrate the fabrication of nano-architected materials via scalable self-assembly processes with features that span across multiple scales—from nanometers to centimeters. Through experiments and simulations, we show that the smooth, doubly curved, shell-based geometries achieved through this process can surpass truss-based architectures in terms of energy absorption, stiffness-to-density response, and especially, mechanical resilience through an unprecedented combination of material size effects and optimal topology.

Author contributions: C.M.P., J.R.G., and D.M.K. designed research; C.M.P., A.V., S.K., T.W., and D.W.Y. performed research; C.M.P. contributed new reagents/analytic tools; C.M.P. and T.W. analyzed data; and C.M.P., J.R.G., and D.M.K. wrote the paper.

The authors declare no competing interest.

This article is a PNAS Direct Submission.

Published under the PNAS license.

¹To whom correspondence may be addressed. Email: dmk@ethz.ch.

This article contains supporting information online at <https://www.pnas.org/lookup/suppl/doi:10.1073/pnas.1916817117/-DCSupplemental>.

First published March 4, 2020.

via molecular processes like self-assembly of block copolymers (29, 30) or polymeric microemulsions (31–33). These processes not only enable orders of magnitude increase in fabrication volumes (34, 35) compared with additively manufactured materials but also have the potential to expand the parameter space by tailoring architectural features with sizes that range from tens of nanometers to tens of micrometers (e.g., by changes in phase concentrations, molecular weights, or temperature) (36). In addition, nanoscale features bear the advantage of leveraging material-level size effects that were previously shown to equip truss lattices with exceptional strength (2) (but poor resilience).

Here, we combine the best of two approaches—self-assembled double-curvature shell architectures and strong nanoscale material effects—into a class of nanolabyrinthine materials that do not rely on periodicity and provide a promising scalable pathway to low-density architected materials with extremely low weight, high stiffness, and extreme resilience. We demonstrate a self-assembly-based fabrication process that uses natural spinodal decomposition to create templates for doubly curved nanoshell materials with overall sample volumes of up to a few cubic centimeters. To explore the resulting mechanical properties of materials produced via the method described above, we perform a systematic parameter space exploration using computational spinodal decomposition and direct laser writing as prototyping tools that enable repeatable nanomechanical experiments and numerical simulations. Using numerical tools and theory, we provide explanations for the observed extreme recoverability and the predicted stretching-dominated response of these materials, evidencing clear mechanical advantages over truss- or plate-based architected materials.

Self-Assembly-Based Fabrication

Our fabrication strategy (Fig. 1A) harnesses the self-assembly capabilities of polymeric emulsions to create bicontinuous, doubly curved shell-based materials with throughput volumes on the order of cubic centimeters. With pore sizes on the order of tens of micrometers and smooth walls with thicknesses on the order of tens of nanometers, our materials span six orders of magni-

tude from the smallest feature dimension to the overall sample dimensions and present a realization of a scalable self-assembled nanoshell-architected material. We fabricated the porous bicontinuous template (Fig. 1B) by exploiting the spinodal decomposition of an epoxy-based emulsion (*Materials and Methods*), which produced a fully interconnected, nominally isotropic solid phase of relative density $\bar{\rho} \approx 44\%$ (i.e., fill fraction) upon polymerization with consistent pore morphologies on the order of tens of micrometers (32). This template was coated with a 79-nm conformal coating of atomic-layer deposition (ALD)-deposited Al_2O_3 followed by O_2 plasma ashing to remove the epoxy template and yield the resulting nanolabyrinthine shell-based material. The polymerization-induced phase separation process that creates the initial bicontinuous templates gives these nanolabyrinthine materials the potential to be fully tunable using thermal, chemical, or mechanical stimuli during self-assembly (32, 37, 38), which leads to controllable morphologies for tailoring material properties.

Parameter Space Exploration

To enable a systematic exploration of the wide design space achievable through the general fabrication concept demonstrated in Fig. 1B, we fabricated repeatable samples at the microscale with geometries that were computed to match the characteristics of the larger self-assembled samples.

Simulation of the Self-Assembly Process. To computationally arrive at the bicontinuous morphologies, we described the phase separation process during self-assembly of a generic two-phase system using a Cahn–Hilliard-type phase field model (39) in which $\varphi(\mathbf{X}, t) \in [0, 1]$, defined at position \mathbf{X} and time t , separates solid ($\varphi = 1$) from void ($\varphi = 0$) domains. To control the characteristics of the resulting porous bicontinuous microstructures, we fix the average fill fraction at 50% and tune the surface energy of the interface between the two phases to modify the resulting feature morphology. Drawing inspiration from nanoporous foams and block copolymers with morphology and directionality that can be controlled by properly choosing the alloying

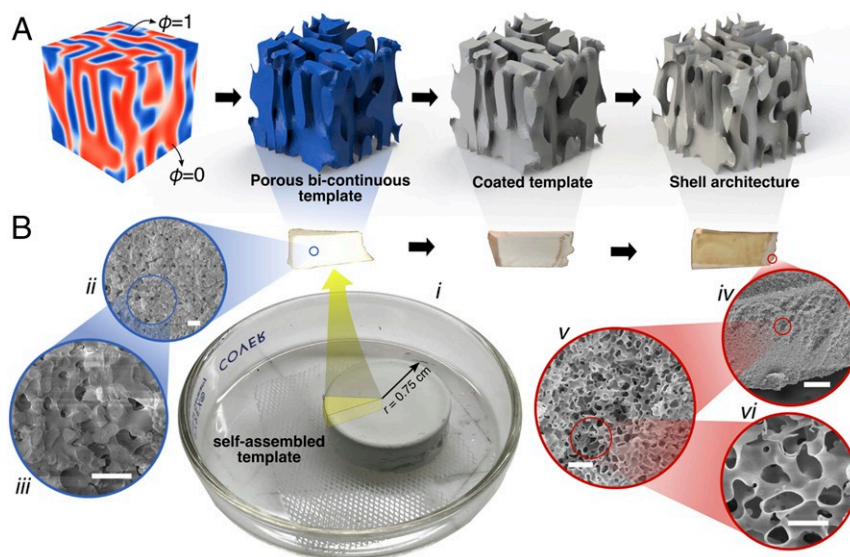


Fig. 1. Self-assembled nanolabyrinthine shell-based material. (A) Schematic of the fabrication process starting with spinodal decomposition of an epoxy resin ($\phi = 1$) and PEG ($\phi = 0$) emulsion, which is thermally cured to produce a porous bicontinuous template after extraction of PEG. The template is then conformally coated with ALD Al_2O_3 , which after removing the epoxy phase via O_2 plasma ashing, composes the resulting nanolabyrinthine shell architectures. (B, i) Photograph of a self-assembled porous epoxy disk fabricated using the process described above. (B, ii and iii) SEM micrographs of a wedge extracted from the disk. (B, iv to vi) SEM micrographs of the wedge after coating with 79 nm of ALD Al_2O_3 and removal of the epoxy, yielding the shell-based nanolabyrinthine material. (Scale bars: B, ii and iii, 10 μm ; B, iv, 100 μm ; B, v, 10 μm ; B, vi, 5 μm .)

(40, 41) or mixing ratios (42), we computed anisotropic shell architectures that mimic such directional tunability (43). Specifically, we prescribed an anisotropic surface energy $\gamma(\mathbf{n})$ as a function of the surface normal \mathbf{n} to penalize growth along a particular set of directions defined by $\{\mathbf{m}_1, \dots, \mathbf{m}_n\}$, which produces bicontinuous shapes that are arranged in energetically favorable directions perpendicular to the \mathbf{m}_i directions and possess, in principle, any prescribed elastic symmetry. The resulting average pore size and the interface curvatures can be further controlled by the (simulated) duration of the phase separation process. Conformally coating the computed solid phase with a thin layer of a stiff material (with thickness that is uniform and below 10% of the average feature size), subsequently removing the solid phase, creates the sought thin-shell architectures corresponding to the collective union of all interface regions. For instance, *SI Appendix, Fig. S1* depicts the resemblance of the computed isotropic shell architecture (i.e., no preferential directions \mathbf{m}_i) to the self-assembled sample from Fig. 1B.

Fabrication of Microscale Prototypes. We fabricated representative examples of the computed architectures out of thin-shell alumina using a three-step process: 1) two-photon lithography direct laser writing (Nanoscribe GmbH) to create three-dimensional (3D) scaffolds with prescribed shapes out of IP-Dip photoresist; 2) ALD of 11-, 44-, or 168-nm-thick conformal coatings of Al_2O_3 onto the scaffolds; and 3) removing polymer templates by selectively etching small perforations in the coating using a focused ion beam (FIB) and ashing the samples in O_2 plasma. Details of this fabrication process are provided in *Materials and Methods* and in *SI Appendix, Fig. S2*. The resulting nanolabyrinthine sample form factors were cubic, with overall dimensions of $125 \times 125 \times 125 \mu\text{m}^3$, and porous feature sizes on the order of $\sim 10 \mu\text{m}$ akin to the pores of nanolabyrinthine samples from Fig. 1B. The thus-produced samples had a relative density $\bar{\rho}$ of ~ 0.15 to 2.4%, which corresponds to 4 to 62 mg/cm^3 depending on shell thickness. Five representative examples that showcase the wide range of self-assembly-like architectures are shown in Fig. 2. The scanning electron microscopy (SEM) images include columnar (Fig. 2A), lamellar (Fig. 2C), isotropic (Fig. 2D), cubic (Fig. 2E), and trigonal (Fig. 2F) architectures with direction-dependent mechanical properties that vary strongly across architectures.

Tunable Elastic Anisotropy. The mechanical anisotropy of such shell-based architectures is highlighted by the elastic surfaces (Fig. 2), which convey the orientation-dependent sample stiffness (i.e., Young's modulus E as a stiffness measure against uniaxial loading) calculated using linear elastic shell finite element models with the constituent properties of ALD Al_2O_3 (44) (*Materials and Methods*). We first simulated uniaxial compression of each architecture along the [100], [010], and [001] directions, resembling actual experimental boundary conditions, to allow comparison with experimental anisotropy values in those three directions. Additionally, we implemented a homogenization scheme with periodic boundary conditions to calculate the modulus in all directions, first obtaining the full elastic modulus tensor \mathbb{C} and then extracting the compliance tensor $\mathbb{S} = \mathbb{C}^{-1}$, which provided E along arbitrary directions. The resulting elastic surface plots are normalized by the Young's modulus of ALD alumina, E_s , and colors represent the magnitude of the normalized modulus (Fig. 2B, *Insets*). The deviation of elastic surfaces from spherical shape is quantitatively related to the elastic anisotropy and is typically maximized along directions perpendicular to the preferential \mathbf{m} vectors.

Fig. 2B shows two ellipsoidal lobes along the [001] direction that comprise the elastic surface of the columnar architecture shown in Fig. 2A along with two further elastic surfaces for reference: that of an octet truss lattice [one of the most extensively explored stiffer periodic architectures (1, 10, 11, 45)] represented

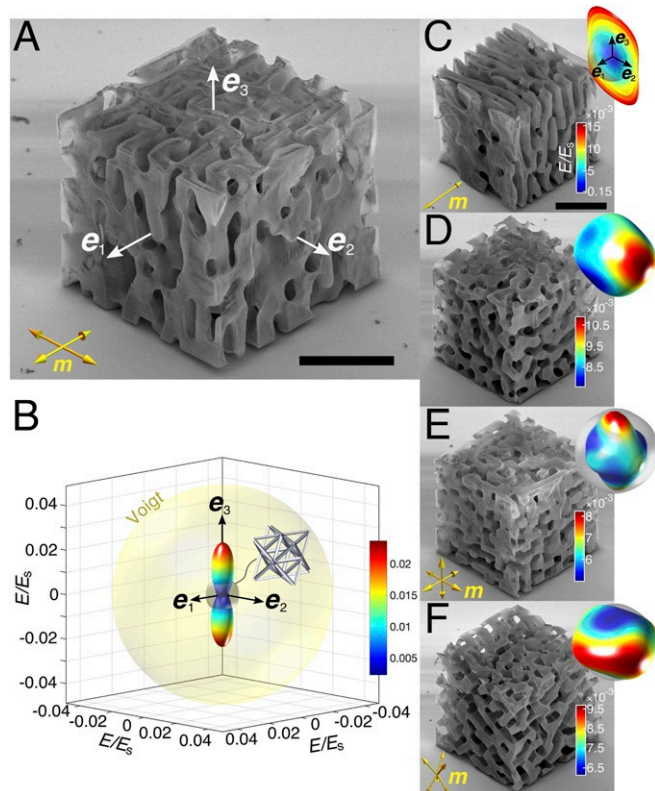


Fig. 2. Anisotropic Al_2O_3 shell-based bicontinuous geometries. (A) Columnar shell geometry with 11-nm shell thickness and (B) corresponding elastic surface at $\bar{\rho} = 4.8 \pm 0.3\%$ showing the computed anisotropy as compared with that of an equally dense octet truss (gray surface). (C) Lamellar, (D) isotropic, (E) cubic, and (F) trigonal geometries with the corresponding elastic surfaces as *Insets* (same $\bar{\rho}$ as in B). The Voigt bound of $E/E_s = 0.048$ is presented as a golden spherical surface. When not visible, the octet elastic surface is contained within the bicontinuous material's surface. The preferential \mathbf{m} vectors are depicted where applicable. (Scale bar: 50 μm .)

by a small gray surface centered at the origin and that of the Voigt theoretical upper bound (46) (defined by the rule of mixtures between Al_2O_3 and air) shown as a golden sphere. This plot reveals that, for this representative case of $\bar{\rho} = 4.8 \pm 0.3\%$, the maximum elastic modulus of the columnar architecture outperforms the equivalently lightweight octet truss by a factor of 3.6 and reaches 48% of the Voigt bound. This particular relative density was chosen for comparison since here, the elastic surface of the hollow octet resembles that of the classic solid-beam octet, and those of the nanolabyrinthine architectures remained representative of the fabricated relative densities (*SI Appendix, Fig. S3*). The contoured elastic surfaces also reveal a stiff omnidirectional response in the absence of preferential directions within the architecture, an example of which is shown in Fig. 2D, where the architecture's response is close to isotropic as would be the case, for example, in nanoporous materials (47) and stochastic foams (28). The elastic surface of the octet is fully contained within that of the isotropic shell architecture (Fig. 2D), which demonstrates that the nonperiodic bicontinuous architectures in this work can be stiffer in all directions than an equally dense periodic truss architecture, with improvements of up to 61% along particular directions (*SI Appendix, Fig. S4*). The columnar (Fig. 2A), lamellar (Fig. 2C), cubic (Fig. 2E), and trigonal (Fig. 2F) geometries reflect the wide range of mechanical anisotropy achievable by tuning the shell geometries.

In the case of the columnar architecture, the anisotropy induced by the selected preferential directions promotes material arrangement in stress-bearing columnar features along the

[001] direction, which renders its relative modulus E/E_s in this direction the highest for all studied geometries. The lamellar structure (Fig. 2C) displays the highest degree of anisotropy, with an $E_{[001]}/E_{[100]}$ ratio of 177, driven by sheet-like, low-interconnectivity material arrangements along the [010] and [001] directions. These computational results demonstrate that introducing preferential directions into the nonperiodic shell architectures allows for prescribing substantial elastic anisotropy and provides a mechanism to design the elastic response along chosen directions in a single material, attaining performance superior to some periodic architectures. As expected, all computed elastic responses are below the theoretical upper bound (since enforcing shell bicontinuity requires some material arrangement in less than ideal configurations), yet the surface energy-driven connectivity is achieved without any sharp junctions or edges—contrary to what is typical in most periodic architectures—and is essential in giving these nanolabyrinthine materials exceptional properties beyond stiffness.

To test the computational predictions, we conducted uniaxial compression experiments on each architected sample along their $\langle 100 \rangle$ directions in a nanoindenter (G200 XP; KLA) with a flat punch tip to strains of $\varepsilon = 35\%$ at a quasistatic rate of $\dot{\varepsilon} = 10^{-3} \text{ s}^{-1}$. We compressed a minimum of three samples for each configuration (defined by geometry, orientation, and shell thickness) and converted the recorded load vs. displacement data into stresses and strains by normalizing by the sample footprint area and height, respectively. We obtained the effective elastic modulus $E_{[i]}^*$ and material strength $\sigma_{y,[i]}^*$ from the stress–strain data as the slope of the linear loading regime and the load at the onset of nonlinearity, respectively (*Materials and Methods*). Representative stress vs. strain datasets are shown in *SI Appendix, Fig. S5*, and they reveal the characteristic linear and nonlinear responses of samples at the three different shell thicknesses. *SI Appendix, Fig. S6C* shows that the representative 168-nm shell thickness samples ($\bar{\rho} = 2.3 \pm 0.1\%$) exhibited the predicted two orders of magnitude anisotropy for the lamellar architecture, with an experimental $E_{[100]}^*/E_{[001]}^*$ ratio of 0.057 compared with 0.014 predicted by simulations. The close to isotropic and columnar samples approximated the numerical models' overall anisotropy with experimental $E_{[001]}^*/E_{[100]}^*$ ratios of 0.87 and 3.0 compared with the numerical ones of 0.92 and 7.2, respectively. The inherent surface waviness of the samples caused by the layer-by-layer 3D printing process used to perform this exploration slightly undermines the mechanical properties (*SI Appendix, Fig. S7*) but preserves the desired qualitative anisotropic response. Thinner-walled samples (i.e., $t = 11$ and 44 nm) exhibited the same anisotropic behavior and had higher knockdown factors caused by fabrication defects (*SI Appendix, Fig. S6*).

Enabling Extreme Mechanical Resilience

To probe the mechanical resilience of the self-assembly geometries, we performed additional in situ cyclic compressions on selected microscale prototype architectures in a custom nanomechanical instrument inside of an SEM chamber (2) (Quanta 200 FEG; Thermo Fisher). Our experiments reveal that the nanolabyrinthine ceramic architectures possess high and tunable directional stiffness while avoiding the stress concentrations typically found at junctions in most periodic architectures (7, 15, 48, 49), which enables the extraordinary mechanical resilience demonstrated in Fig. 3. The 11-nm-thick samples exhibited full recovery in these in situ experiments, with no visible microcracks, after 10 compressive cycles to strains of up to 35%. This is in contrast to all other thin-walled ceramic and polymer beam-based architected materials at this scale, which fail by forming microcracks at nodes and in which strength and energy absorption hysteresis deteriorate by an order of magnitude or more after only a single load cycle (15, 49, 50). While both hollow beam and

nanolabyrinthine architectures structurally recover due to elastic shell buckling, the nanolabyrinthine samples in this work are the only ones that do not visibly fracture and maintain substantial mechanical performance with cycling.

For instance, the columnar architecture (Fig. 3) compressed along the [001] direction exhibited a linear loading regime followed by the onset of elastic buckling of the Al_2O_3 shells from a strain of 5 to 10%, beyond which they underwent nonlinear buckling and self-contact, ultimately recovering their original geometry after each cycle as characterized by self-similar hysteretic behavior. We focus our analysis on the response of the columnar geometry since it is representative of the other architectures' hysteretic response while exhibiting the highest strength and stiffness (*SI Appendix, Fig. S8*). This hysteresis—observed in all geometries of 11-nm thickness—implies significant energy dissipation, which is attributed to friction and the nonlinear buckling processes without any permanent structural deformation or evident microcrack formation (*Movies S1–S4*). Increasing the shell thickness to 44 nm changed the failure mechanism to mostly fracture dominated with structural recovery enabled by marginal elastic buckling (*Movies S5–S9*), while the 168-nm samples underwent mostly catastrophic failure during the first cycle with their structural integrity compromised (*SI Appendix, Fig. S5* and *Movies S10–S14*). The response of the thicker samples is consistent with the competing effects of elastic buckling and material failure found previously for hollow shell truss architectures (2), while the response of the thinner samples evidences a significant improvement in cyclic degradation when compared with their thin-walled truss counterparts that form microcracks even in the shell buckling regime. The improved cyclic performance of nanolabyrinthine architectures over truss ones is also in line with observations that fillets, a feature to decrease curvature at truss nodes, can be expected to provide improved effective strength even in lattice materials (26).

We attribute the observed mechanical resilience to the unique combination of thin, almost defect-free alumina shells [exploited

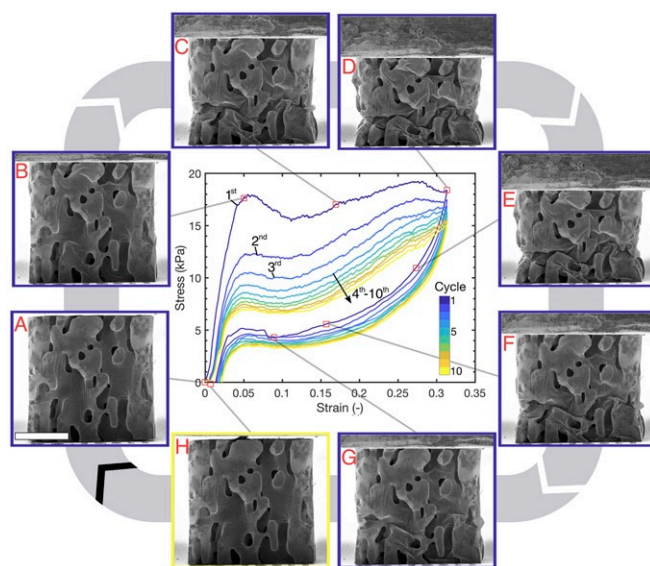


Fig. 3. Cyclic loading and recovery. Cyclic loading of an 11-nm-thick columnar architecture: (A) initial geometry, (B) end of linear regime and onset of buckling, (C) nonlinear buckling regime, (D) end of loading regime, (E–G) unloading regime showing elastic recovery, and (H) final geometry after 10 cycles showing no visible permanent deformation or microcracks. All micrographs correspond to the first cycle except for H, which corresponds to the end of the 10th cycle. (Scale bar: 50 μm .)

previously only in trusses (2)] on the one hand and the low local curvatures in the doubly curved shell architectures on the other hand. The low principal curvatures minimize local stress concentrations, which prevents localized material failure. We quantify the architectural morphology by extracting the pointwise mean and Gaussian curvatures and calculating the principal curvature probability distribution (i.e., the distribution of κ_1 and κ_2 , which are normalized to $\hat{\kappa}_i = \kappa_i L$, where L is the sample dimension) (40). For the columnar architecture, Fig. 4A shows that most of its features have principal curvatures $|\hat{\kappa}_i| < 20$ (other architectures are presented in *SI Appendix*, Fig. S9). Performing the same analysis for an octet truss shows significantly larger curvatures and a bimodal distribution, with a peak curvature dominated by the struts' nonzero κ_2 curvature and another peak at $|\hat{\kappa}_i| \gg 20$ corresponding to the nodal joints. Even after reducing such singularities by introducing finite-sized joint radii (Fig. 4B) by means of fillets with radii $0.5r$ and r (where r is the strut radius), the higher curvatures and the bimodal distributions remain.

As a representative case to highlight the resilience of our nanolabyrinthine architectures, we cyclically loaded columnar samples along the [001] direction (this is the stiffest of all tested samples and directions so that we generally do not expect soft, compliant deformation modes to engage). To compare the cyclic performance with that of hollow tube octet lattices, we fabricated $5 \times 5 \times 5$ octet tessellations with the same alumina wall thickness and relative density as the 11-nm nanolabyrinthine samples and performed the same in situ cyclic compressions along the [001] direction (*SI Appendix*, Fig. S10 and *Movie S15*). We tracked the degradation of the measured modulus E_i^* , strength $\sigma_{y,i}^*$, and the absorbed energy density $\psi_i = \frac{1}{2} \oint_i \sigma d\epsilon$, graphically represented as the enclosed area in the stress-strain response for a given i th cycle.

Fig. 4C summarizes how these three performance metrics, normalized by their values in the first cycle, evolved over 10 load

cycles. These plots convey that, between the first and second cycles, the energy absorption decreased by 27% for the columnar architecture and by 58% for the octet, asymptotically approaching the 10th-cycle limit of 38% of the original energy storage capacity for the columnar and 14% for the octet architectures. Young's modulus showed a second-cycle drop of 15% for the columnar architecture compared with 63% for the octet. This significant drop in the octet's mechanical response is caused by the localized material failure and a loss of load-bearing capacity at multiple nodes, the number of which increases with cycling. The less than half relative drop in energy absorption and a factor of three-lower reduction in Young's modulus between first and second cycles of the columnar architectures, when compared with octets, likely stem from internal microcracks and variations in the self-contact process that weaken but not necessarily disable load-bearing shells (no cracks were observed on the structure's outer surfaces). Strength performance also seems to be superior for the columnar architecture, showing a first- to second-cycle degradation of 24% compared with 70% for the octet, with the absolute strengths being greater than those of octet beyond the second cycle. Despite the knockdown factor in stiffness and strength caused by shell waviness (*SI Appendix*, Fig. S7), the columnar architecture shows considerably superior mechanical performance compared with the periodic truss architecture through (at least) 10 cycles. Since the deformation mechanisms exhibited by the columnar and octet architectures are representative of nanolabyrinthine and periodic truss architectures, respectively, the benefits of nonperiodic, low-curvature shells can be harnessed to produce architected nanolabyrinthine materials with mechanical resilience superior to that of an equivalent junction-based truss (or plate) architecture. In particular, the nonperiodic nature of similar doubly curved shell structures has been shown to provide insensitivity to imperfections (28) at higher relative densities, providing another advantage over thick-shell periodic truss architectures.

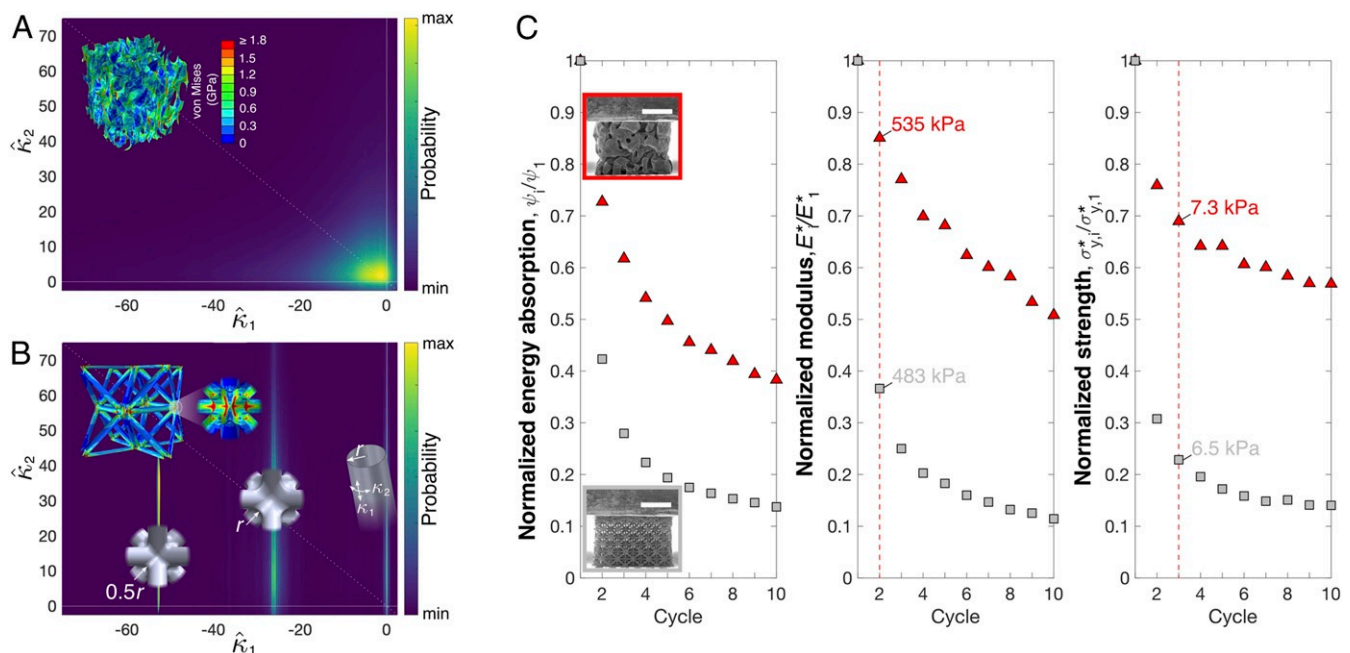


Fig. 4. Curvature distribution and cyclic mechanical performance. (A) Dimensionless curvature probability distribution for the columnar bicontinuous architecture with the stress distribution for uniaxial loading (*Inset*), $\hat{\kappa}_i = \kappa_i L$, where L is the sample characteristic dimension. (B) Two octet architectures with fillets of radii $0.5r$ and r , where r is the strut radius, and stress distribution for the $0.5r$ case in uniaxial loading (*Inset*; same color map as A). The normalized curvatures are defined as $\hat{\kappa}_i = \kappa_i L$, where κ_i is a principal curvature and L is the unit cell dimension. (C) Evolution of first cycle-normalized mechanical properties through cyclic loading for hollow octet and columnar bicontinuous material of relative density $\bar{\rho} = 0.15\%$ and 11-nm shells. *Insets* depict both architectures at maximum compression in an in situ experiment. (Scale bar: *Insets*, 50 μm .)

Superior Stiffness vs. Density Parameter Space

The ALD process used in this work allowed for a wide range of shell thicknesses from 11 to 168 nm, which enabled the nanolabyrinthine architectures to span a relative density range from 0.15 to 2.4%. To explore the effect of relative density on stiffness and anisotropy, we performed finite element simulations of three types of architectures with the same relative densities: columnar nanolabyrinthine, hollow octet truss, and the Schwarz Primitive TPMS (18). Fig. 5 shows the normalized elastic modulus $E_{[001]}/E_s$ (Fig. 5, *Upper*) as a function of relative density for these three architectures along with their elastic surfaces at three different relative densities (Fig. 5, *Lower*). These simulations demonstrate a close to constant anisotropy for the columnar architecture (Fig. 5, red), with virtually identical lobular elastic surfaces, and a quasilinear stiffness scaling exponent of $\alpha = 1.17$ (fit of the type $E_{[1]} \propto \bar{\rho}^\alpha$) at relative densities below 5%. The TPMS (Fig. 5, blue) and octet (Fig. 5, gray) geometries exhibit significant transformations in anisotropy, both having a scaling exponent of ~ 1.4 and with the octet gradually changing its direction of maximal stiffness from $[001]$ to $[111]$ throughout the studied relative density regime. This anisotropy in trusses arises from the competing effects of beam bending and stretching (51) and presents an additional challenge when designing truss-based materials. Nanolabyrinthine architectures hence seem immune to significant changes in wall thickness as they retain their target elastic anisotropy throughout the full explored density range.

The stiffness scaling of our nanolabyrinthine architectures reveals another counterintuitive feature, previously shown only for thick polymeric shells (28): all architectures display an almost linear stiffness scaling with relative density. Performing the same analysis for the rest of the nanolabyrinthine architectures was consistent with the stiffness scaling of the columnar one with scaling exponents ranging from 1.16 to 1.22 in the $\langle 100 \rangle$ directions

(*SI Appendix, Fig. S11*), remaining below the scaling exponents computed for the TPMS and octet architectures. Linear scaling is considered to be optimal as it corresponds to the rule of mixtures and is generally associated with stretching as the primary deformation mechanism; bending manifests in an exponent of $\alpha = 2$. Although the double-curvature morphology explains the enhanced resilience observed for all architectures, the fact that their elastic deformation is stretching dominated seems counterintuitive at first—but is also tied to the double curvature. In the limit of very thin shells of thickness t , the bending stiffness (scaling with t^3) is comparably less than the stretching stiffness (scaling with t) so that membrane theory effectively describes the deformation behavior.

The effect of double curvature on the load distribution in thin elastic shells is best elucidated by the thought experiment of approximating, for example, the columnar topology as 1) an array of ideal cylindrical shells with $\kappa_1 = 0$ and $\kappa_2 > 0$ having zero Gaussian curvature (i.e., $\kappa_1 \kappa_2 = 0$), 2) an array of doubly curved barreled, nearly cylindrical shells with $\kappa_1 > 0$ and $\kappa_2 > 0$ having positive Gaussian curvature, and 3) an array of doubly curved waisted, nearly cylindrical shells with $\kappa_1 < 0$ and $\kappa_2 > 0$ having negative Gaussian curvature (*SI Appendix, Fig. S12*). The curvature distribution presented in Fig. 44 demonstrates that the negative Gaussian curvature case is closest to the present shell architectures. For a perfectly cylindrical shell ($\kappa_1 \kappa_2 = 0$) of low thickness (therefore, bending is negligible, and membrane theory applies), axial loads distributed across the end perimeters produce axial inner stresses that are constant along straight vertical lines, analogous to an arrangement of straight rods. In the nearly cylindrical case with negative Gaussian curvature, the shell solution still reveals straight (but no longer vertical) isostress characteristics that carry constant axial loads (52) (*SI Appendix*). In these two cases, the effective axial response is akin to that of an assembly of rods, thus being stretching

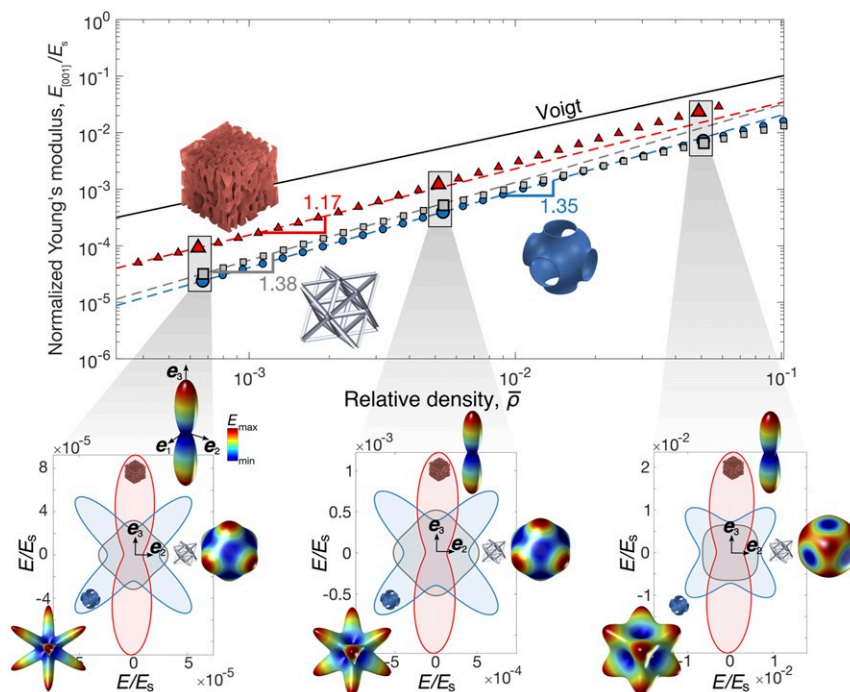


Fig. 5. Stiffness scaling and elastic surface variations. Normalized Young's modulus $E_{[001]}/E_s$ as a function of relative density $\bar{\rho}$ for bicontinuous columnar (red), Schwarz Primitive TPMS (blue), and hollow octet (gray) architectures. Regression fits for the 10 lowest relative densities from each architecture are depicted as dashed lines, assuming a relation $E_{[1]}/E_s = C \bar{\rho}^\alpha$, with the corresponding scaling exponent α shown next to each fit. The elastic surfaces for each structure along with their two-dimensional projections are shown for three selected relative densities. Close to constant anisotropy is observed for the bicontinuous architecture as opposed to the TPMS and octet geometries.

dominated and showing optimal scaling. This is in contrast to the waisted, positive-Gaussian cylinder, which diffuses concentrated axial end loads inhomogeneously throughout the shell, in turn demonstrating that the negative Gaussian curvature adds rigidity to axial loads in the form of a membrane stress-carrying ability (52, 53). Simulation results for those elementary cylindrical structures are depicted in *SI Appendix, Fig. S12*, which also shows vertically aligned force chains in a uniaxially compressed columnar architecture along which the principal stresses are nondecaying and maximal, resembling the nondecaying solution of the waisted cylindrical shells (52, 53). Given that this solution only applies while the membrane hypothesis is valid (i.e., small thicknesses and relative densities), it is expected that bending will take a more prominent role at higher relative densities, yielding slightly higher scaling exponents due to less ideal stress distributions.

Conclusion

We developed a fabrication method that enables self-assembly of nonperiodic, shell-based nano-architected materials, with features on the order of nanometers and overall volumes of up to cubic centimeters. Using additive manufacturing synthesis, in situ experiments, and theory as exploratory tools, we showcase mechanical tunability and unsurpassed resilience of 0.15%-dense ceramic nanolabyrinthine shell architectures. The proposed self-assembly method presents a significant departure from existing fabrication and design principles to create architected materials at any scale because it bypasses the restrictions of commonly practiced slow and defect-prone additive manufacturing techniques. These nanolabyrinthine ceramic shell architectures overcome the inevitable high-stiffness, high-resilience exclusivity and maintain controllable and constant anisotropy over a wide range of relative densities, shown here from 0.15 to 2.4%. This was achieved by combining two beneficial design strategies explored only independently before: extremely thin shells with size that is in the regime of nanomaterial size effects and failure suppression as well as smooth double-curvature structural architectures that provide high stiffness. This enables producing architected materials with high and tunable stiffness, high resilience, and potential for scalable fabrication at large volumes through self-assembly.

Materials and Methods

Self-Assembly Sample Fabrication. The centimeter-scale bicontinuous polymer was synthesized according to the method reported by Tsujioka et al. (32). In brief, 2.34 g of diglycidyl ether of bisphenol A, 0.86 g of 4,4'-methylenebis(cyclohexylamine), and 8.01 g of polyethylene glycol (PEG) 200 were added to a 20-mL vial; mixed vigorously in a vortex mixer to form a clear homogenous solution; and then, ultrasonicated for 10 s to remove any bubbles formed. Then, 1.5 mL of this solution was added to a 1-dram vial (15-mm diameter) and cured at 130 °C for 3 h to form a white solid. After polymerization, the sample was immersed in water for 24 h to extract out the PEG 200 porogen followed by drying in vacuum at room temperature for another 24 h. The polymer was then sectioned, and the inner cores were conformally coated in Al₂O₃ using an ALD process (Cambridge Nanotech S200). The chamber was held at 150 °C with a recipe consisting of pulsing H₂O for 15 ms, purging for 20 s, pulsing trimethyl aluminum for 15 ms, purging again for 20 s, and repeating the process for the desired layer thickness. The system was run for 750 cycles (corresponding to 79 nm) with N₂ as the carrier gas at a flow rate of 20 sccm. The coating thickness was verified via spectroscopic ellipsometry using an alpha-SE Ellipsometer (J. A. Woollam Co., Inc). To expose the epoxy component after coating, we made sacrificial cuts on some edges using a razor. The exposed samples were inserted in an O₂ plasma asher between 100 and 200 h in a 300-sccm flow rate at 100-W power output until the epoxy component was fully removed.

Microscale Sample Fabrication. The computed geometries were fabricated at the microscale using a two-photon lithography process in a Photonic Professional GT system (Nanoscribe GmbH). Laser power was 15 mW, and scan speed was 10 mm s⁻¹ on an IP-Dip photoresist. To prevent excessive warping during the developing process, we dried the samples using a critical point drying process in an Autosamdri-931 system (Tousimis). Following the dry-

ing process, the samples were conformally coated in Al₂O₃ using the ALD process described above. Depending on the sample, the system was run for 100, 400, or 1,600 cycles. After deposition, we introduced perforations on the top ceramic coating using FIB milling in an FEI Nova 200 Nanolab system (*SI Appendix, Fig. S1*). The exposed samples were inserted in an O₂ plasma asher between 80 and 100 h in a 300-sccm flow rate at 100-W power output. Using a high imaging voltage (~10 kV) in a scanning electron microscope, it was possible to determine when the totality of the polymer had been removed.

Computational Framework. The sample geometries were computed using a numerical framework adopted from Vidyasagar et al. (39). In this approach, binary phase separation by spinodal decomposition is modeled using a phase field description, which solves the Cahn–Hilliard equation (in the presence of anisotropic surface energy) for an order parameter field $\phi(\mathbf{x}, t)$ on a 3D representative volume element (RVE) with periodic boundary conditions. The phase field was simulated to evolve from a random initial distribution (with the target mean volume fractions) into solid phase ($\phi = 1$) and void phase ($\phi = 0$) using a stabilized Fourier spectral technique. The Ginzburg–Landau form of the binary potential ensured that the mixture undergoes reverse diffusive processes and formed two stable phases. The interface energy introduced anisotropy by penalizing normal gradients along particular directions \mathbf{m}_i under the presence of an intrinsic length scale ϵ , which determined the pore sizes. This length scale was chosen such that the average pore size was approximately one order of magnitude smaller than the RVE dimension and sufficient representative features were contained within the RVE. Achieving this separation of scales ensured that RVEs of the same fill fraction ϕ but different randomized initial conditions exhibited the same homogenized response such that a single RVE could be used for each (an)isotropy condition without loss of generality (39). The stabilization and regularization of the Fourier spectral method, which was chosen to exploit the computational efficiency of fast Fourier transforms, ensured that interfacial ringing artifacts were largely mitigated (by using finite difference stencils in real space to obtain asymptotically consistent acoustic wave vectors). Simulations were initiated with smooth initial Gaussian distributions for probabilistic pattern formation and evolution. The collection of all interfaces resulting from the simulated demixing process (i.e., those defined by $\phi = 0.5$) was extracted to yield the geometries used to generate the (an)isotropic nanolabyrinthine architectures. The resulting RVEs contained periodic boundaries, although the internal geometries lacked symmetry and periodicity due to the employed Fourier transform-based spectral simulation technique.

The geometries derived from the computational spinodal decomposition process were meshed using three-node shell elements (S3R) in Abaqus (Simulia). A mesh convergence study was performed to ensure mesh-independent results, which led to models containing ~237,000 to 266,000 elements, depending on architecture type. Following an analogous mesh convergence study, the octet and TPMS architectures were meshed to result in a total of 16,000 and 63,000 elements, respectively. To compare the response of uniaxial compression experiments with simulations, we performed linear perturbation simulations to establish the linear response of each architecture. For each direction of interest, we applied a compression strain of 1% by constraining the out-of-plane displacement degrees of freedom (dofs) on opposite faces of the finite element representation of a given sample RVE while leaving the in-plane displacement dofs and all rotational dofs on those two faces unconstrained. The remaining four faces of the cube-shaped RVE were left unconstrained as in experiments. To predict the full elastic response of an architecture (i.e., the elastic surfaces revealing Young's modulus in all possible 3D directions), we implemented a computational homogenization scheme. By applying periodic boundary conditions, we imposed average strains within the RVE. Specifically, we sequentially imposed six linearly independent choices of the infinitesimal (symmetric) strain tensor ϵ and computed the resulting average RVE stress tensor σ . The full elastic modulus tensor \mathbb{C} was then obtained from Hooke's law $\sigma = \mathbb{C}\epsilon$ of linear elasticity (or $\sigma_{ij} = C_{ijkl}\epsilon_{kl}$ with the fourth-order elastic stiffness tensor \mathbb{C} using Einstein's summation convention). Lastly, the compliance tensor $\mathbb{S} = \mathbb{C}^{-1}$ was calculated to obtain Young's modulus $E(\mathbf{d})$ in any direction \mathbf{d} as $E^{-1}(\mathbf{d}) = \mathbb{S}_{ijkl}d_id_jd_kd_l$.

Nanomechanical Experiments. We performed nanomechanical experiments on the shell-based architectures to determine their effective stiffness, strength, and recoverability along the $\langle 100 \rangle$ directions. We performed ex situ uniaxial compression experiments on a minimum of three samples per configuration (i.e., each geometry, thickness, and orientation) using a G200

XP Nanoindenter (KLA). The samples were compressed to strains of up to $\epsilon = 35\%$ at a strain rate of $\dot{\epsilon} = 10^{-3} \text{ s}^{-1}$ using a 400- μm flat punch tip. The in situ compressions were performed using an inSEM II Nanoindenter (Nanomechanics) under the same conditions as in the ex situ compressions. Cyclic compressions of up to 10 cycles were performed in situ to observe the failure mechanisms and to quantify the cycle-specific dissipated energy and recovery. For all experiments, the effective Young's modulus was approximated by the loading slope of each cycle's linear stress-strain regime. For samples exhibiting catastrophic failure (i.e., some of the 44-nm samples and all of the 168-nm samples), the strength was approximated as the maximum

load prior to collapse. For the recoverable samples (i.e., some of the 44-nm samples and all of the 11-nm samples), the strength was calculated via the 0.2% strain offset method.

Data Availability. All data needed to evaluate the conclusions in this paper are available in the text or in [SI Appendix](#).

ACKNOWLEDGMENTS. We acknowledge financial support from Office of Naval Research Award N00014-16-1-2431. J.R.G. acknowledges support from the Vannevar Bush Faculty Fellowship.

1. X. Zheng *et al.*, Ultralight, ultrastiff mechanical metamaterials. *Science* **344**, 1373–1377 (2014).
2. L. R. Meza, S. Das, J. R. Greer, Strong, lightweight, and recoverable three-dimensional ceramic nanolattices. *Science* **345**, 1322–1326 (2014).
3. X. Zheng *et al.*, Multiscale metallic metamaterials. *Nat. Mater.* **15**, 1100–1106 (2016).
4. J. Bauer, A. Schroer, R. Schwaiger, O. Kraft, Approaching theoretical strength in glassy carbon nanolattices. *Nat. Mater.* **15**, 438–443 (2016).
5. T. A. Schaedler *et al.*, Ultralight metallic microlattices. *Science* **334**, 962–965 (2011).
6. X. Zhang, A. Vyatskikh, H. Gao, J. R. Greer, X. Li, Lightweight, flaw-tolerant, and ultrastrong nanoarchitected carbon. *Proc. Natl. Acad. Sci. U.S.A.* **116**, 6665–6672 (2019).
7. A. J. Mateos, W. Huang, Y. W. Zhang, J. R. Greer, Discrete-continuum duality of architected materials: Failure, flaws, and fracture. *Adv. Funct. Mater.* **1806772**, 1806772 (2018).
8. T. Tancogne-Dejean, A. B. Spierings, D. Mohr, Additively-manufactured metallic micro-lattice materials for high specific energy absorption under static and dynamic loading. *Acta Mater.* **116**, 14–28 (2016).
9. S. Krödel, C. Daraio, Microlattice metamaterials for tailoring ultrasonic transmission with elastoacoustic hybridization. *Phys. Rev. Appl.* **6**, 064005 (2016).
10. L. R. Meza *et al.*, Reexamining the mechanical property space of three-dimensional lattice architectures. *Acta Mater.* **140**, 424–432 (2017).
11. C. M. Portela, J. R. Greer, D. M. Kochmann, Impact of node geometry on the effective stiffness of non-slender three-dimensional truss lattice architectures. *Extreme Mech. Lett.* **22**, 110–138 (2018).
12. L. Liu, P. Kamm, F. García-Moreno, J. Banhart, D. Pasini, Elastic and failure response of imperfect three-dimensional metallic lattices: The role of geometric defects induced by selective laser melting. *J. Mech. Phys. Solid.* **107**, 160–184 (2017).
13. M. S. Pham, C. Liu, I. Todd, J. Lertthanasarn, Damage-tolerant architected materials inspired by crystal microstructure. *Nature* **565**, 305–311 (2019).
14. A. Gross, P. Pantidis, K. Bertoldi, S. Gerasimidis, Correlation between topology and elastic properties of imperfect truss-lattice materials. *J. Mech. Phys. Solid.* **124**, 577–598 (2019).
15. N. G. Dou, R. A. Jagt, C. M. Portela, J. R. Greer, A. J. Minnich, Ultralow thermal conductivity and mechanical resilience of architected nanolattices. *Nano Lett.* **18**, 4755–4761 (2018).
16. J. B. Berger, H. N. Wadley, R. M. McMeeking, Mechanical metamaterials at the theoretical limit of isotropic elastic stiffness. *Nature* **543**, 533–537 (2017).
17. T. Tancogne-Dejean, M. Diamantopoulou, M. B. Gorji, C. Bonatti, D. Mohr, 3D plate-lattices: An emerging class of low-density metamaterial exhibiting optimal isotropic stiffness. *Adv. Mater.* **30**, 1803334 (2018).
18. B. D. Nguyen, S. C. Han, Y. C. Jung, K. Kang, Design of the P-surfaced shellular, an ultra-low density material with micro-architecture. *Comput. Mater. Sci.* **139**, 162–178 (2017).
19. V. Pini *et al.*, How two-dimensional bending can extraordinarily stiffen thin sheets. *Sci. Rep.* **6**, 1–6 (2016).
20. A. Lazarus, H. C. B. Florijn, P. M. Reis, Geometry-induced rigidity in nonspherical pressurized elastic shells. *Phys. Rev. Lett.* **109**, 144301 (2012).
21. U. Nath, B. C. W. Crawford, R. Carpenter, E. Coen, Genetic control of surface curvature. *Science* **299**, 1404–1407 (2003).
22. S. C. Han, J. W. Lee, K. Kang, A new type of low density material: Shellular. *Adv. Mater.* **27**, 5506–5511 (2015).
23. C. Bonatti, D. Mohr, Mechanical performance of additively-manufactured anisotropic and isotropic smooth shell-lattice materials: Simulations & experiments. *J. Mech. Phys. Solid.* **122**, 1–26 (2016).
24. O. Al-Ketan *et al.*, Microarchitected stretching-dominated mechanical metamaterials with minimal surface topologies. *Adv. Eng. Mater.* **20**, 1800029 (2018).
25. L. Zhang *et al.*, Energy absorption characteristics of metallic triply periodic minimal surface sheet structures under compressive loading. *Addit. Manuf.* **23**, 505–515 (2018).
26. R. M. Latture, M. R. Begley, F. W. Zok, Design and mechanical properties of elastically isotropic trusses. *J. Mater. Res.* **33**, 249–263 (2018).
27. J. Biener *et al.*, Size effects on the mechanical behavior of nanoporous Au. *Nano Lett.* **6**, 2379–2382 (2006).
28. M. T. Hsieh, B. Endo, Y. Zhang, J. Bauer, L. Valdevit, The mechanical response of cellular materials with spinodal topologies. *J. Mech. Phys. Solid.* **125**, 401–419 (2019).
29. J. R. Bell, K. Chang, C. R. Lopez-Barron, C. W. Macosko, D. C. Morse, Annealing of cocontinuous polymer blends: Effect of block copolymer molecular weight and architecture. *Macromolecules* **43**, 5024–5032 (2010).
30. S. N. Khaderi *et al.*, The indentation response of Nickel nano double gyroid lattices. *Extreme Mech. Lett.* **10**, 15–23 (2017).
31. F. S. Bates *et al.*, Polymeric bicontinuous microemulsions. *Phys. Rev. Lett.* **79**, 849–852 (1997).
32. N. Tsujioka, N. Ishizuka, N. Tanaka, T. Kubo, K. Hosoya, Well-controlled 3D skeletal epoxy-based monoliths obtained by polymerization induced phase separation. *J. Polym. Sci. Polym. Chem.* **46**, 3272–3281 (2008).
33. N. Zhou, F. S. Bates, T. P. Lodge, Mesoporous membrane templated by a polymeric bicontinuous microemulsion. *Nano Lett.* **6**, 2354–2357 (2006).
34. S. Ndoni, M. E. Vigild, R. H. Berg, Nanoporous materials with spherical and gyroid cavities created by quantitative etching of polydimethylsiloxane in polystyrene-polydimethylsiloxane block copolymers. *J. Am. Chem. Soc.* **125**, 13366–13367 (2003).
35. M. N. Lee, A. Mohraz, Bicontinuous macroporous materials from bijel templates. *Adv. Mater.* **22**, 4836–4841 (2010).
36. T. Vidil, N. Hampu, M. A. Hillmyer, Nanoporous thermosets with percolating pores from block polymers chemically fixed above the order-disorder transition. *ACS Cent. Sci.* **3**, 1114–1120 (2017).
37. D. Zeng, A. Ribbe, R. C. Hayward, Anisotropic and interconnected nanoporous materials from randomly end-linked copolymer networks. *Macromolecules* **50**, 4668–4676 (2017).
38. A. M. Higgins, R. A. L. Jones, Anisotropic spinodal dewetting as a route to self-assembly of patterned surfaces. *Nature* **404**, 476–478 (2000).
39. A. Vidyasagar, S. Krödel, D. M. Kochmann, Microstructural patterns with tunable mechanical anisotropy obtained by simulating anisotropic spinodal decomposition. *Proc. R. Soc. A* **474**, 20180535 (2018).
40. Y. Kwon, K. Thornton, P. Voorhees, Morphology and topology in coarsening of domains via non-conserved and conserved dynamics. *Phil. Mag.* **90**, 317–335 (2010).
41. C. L. Park, J. Gibbs, P. Voorhees, K. Thornton, Coarsening of complex microstructures following spinodal decomposition. *Acta Mater.* **132**, 13–24 (2017).
42. C. Park, J. Yoon, E. L. Thomas, Enabling nanotechnology with self assembled block copolymer patterns. *Polymer* **44**, 6725–6760 (2003).
43. C. R. Lopez-Barron, C. W. Macosko, Direct measurement of interface anisotropy of bicontinuous structures via 3D image analysis. *Langmuir* **26**, 14284–14293 (2010).
44. M. Berdova *et al.*, Mechanical assessment of suspended ALD thin films by bulge and shaft-loading techniques. *Acta Mater.* **66**, 370–377 (2014).
45. V. S. Deshpande, N. A. Fleck, M. F. Ashby, Effective properties of the octet-truss lattice material. *J. Mech. Phys. Solid.* **49**, 1747–1769 (2001).
46. W. Voigt, Ueber die Beziehung zwischen den beiden Elastizitätskonstanten isotroper Körper. *Ann. Phys.* **274**, 573–587 (1889).
47. K. R. Mangipudi, E. Epler, C. A. Volkert, Topology-dependent scaling laws for the stiffness and strength of nanoporous gold. *Acta Mater.* **119**, 115–122 (2016).
48. R. M. Latture, R. X. Rodriguez, L. R. Holmes, F. W. Zok, Effects of nodal fillets and external boundaries on compressive response of an octet truss. *Acta Mater.* **149**, 78–87 (2018).
49. A. Schroer, J. M. Wheeler, R. Schwaiger, Deformation behavior and energy absorption capability of polymer and ceramic-polymer composite microlattices under cyclic loading. *J. Mater. Res.* **33**, 274–289 (2018).
50. L. R. Meza *et al.*, Resilient 3D hierarchical architected metamaterials. *Proc. Natl. Acad. Sci. U.S.A.* **112**, 11502–11507 (2015).
51. T. Tancogne-Dejean, D. Mohr, Elastically-isotropic elementary cubic lattices composed of tailored hollow beams. *Extreme Mech. Lett.* **22**, 13–18 (2018).
52. C. R. Calladine, *Theory of Shell Structures* (Cambridge University Press, Cambridge, UK, 1983).
53. E. Ramm, W. A. Wall, Shell structures - a sensitive interrelation between physics and numerics. *Int. J. Numer. Methods Eng.* **60**, 381–427 (2004).